Results in Physics 16 (2020) 102916

Contents lists available at ScienceDirect

Results in Physics

journal homepage: www.elsevier.com/locate/rinp

Structural and magnetic properties of tailored $NiFe_2O_4$ nanostructures synthesized using auto-combustion method

Rashmi Tiwari[a], Manojit De[a,*], H.S. Tewari[a], S.K. Ghoshal[b]

[a] Department of Pure and Applied Physics, Guru Ghasidas Vishwavidyalaya, Bilaspur, C. G. 495009, India
[b] Advanced Optical Materials Research Group, Physics Department, Faculty of Science, Universiti Teknologi Malaysia, 81310 Skudai, Johor, Malaysia

ARTICLE INFO

Keywords:
Spinel ferrite
XRD pattern
Microstructures
Vibrational spectra
Magnetic properties

ABSTRACT

Spinel ferrite nanoparticles have astounding uses in the diverse field of applications. The virgin nickel ferrite ($NiFe_2O_4$), and cadmium (Cd) and strontium (Sr) substituted nickel ferrite nanostructures were synthesized by a self-ignited auto-combustion method. Such ferrites were characterized at room temperature to determine their composition dependent structural and magnetic properties. XRD patterns revealed cubic spinel single phase. Raman spectra disclosed five active phonon modes assigned to the spinel phase. FTIR spectra of the proposed nanoferrites exhibited two prominent absorption bands allotted to the stretching vibrations of tetrahedral and octahedral complexes. FESEM images manifested the evolution of porous $NiFe_2O_4$ microstructures. Magnetic properties of these ferrites were determined in terms of saturation magnetization, magnetic moment and Y–K angles. The small ratios of remanent to saturation magnetization clearly demonstrated the existence of multi-domains in the grown nanoferrites. The observed enhanced magnetic performance was endorsed to the A-site substitution in the spinel structure.

Introduction

Spinel ferrites have been emerged as potential candidates for diverse applications due to their abundance, flexibility, low-cost and excellent electromagnetic performance over a broad range of frequencies. Generally, the compositional formula of spinel ferrites can be represented by AB_2O_4 (where A is a divalent metallic ion). Based on the cation distribution, spinel ferrites can be categorized into normal, inverse and mixed spinel structures. Earlier, ferrite nanostructures have been intensively utilized for permanent magnets, high-density information storage, and drug delivery. Categorically, nickel ferrite ($NiFe_2O_4$) is a ferrimagnetic material that has low conductivity, low eddy current losses and high electrochemical stability [1,2]. Furthermore, the bulk phase of $NiFe_2O_4$ is fully composed of inverse spinel structures [3].

Researches revealed that the structure and morphology (shape, size and surface topology) of ferrite nanostructures can be controlled accurately by adjusting the composition as well as the methods of syntheses [4,5]. Over the years, diverse techniques have been developed to prepare ferrite nanostructures such as solid-state [6,7], sol-gel [8,9], thermal decompositions [10–12], co-precipitation [13], hydrothermal [14] and mechanical milling [15]. Despite many dedicated efforts, a highly efficient and accurate method for the synthesis of ferrite nanostructures is far from being achieved. On top, the correlation among the compositions, cationic distribution in the structure, electric and magnetic properties of ferrite nanostructures has not been established yet. It is known that eight (8) molecules are involved in the unit cell of $NiFe_2O_4$, wherein a face-centered cubic (FCC) structure is formed by 32 O^{2-} with the availability of 64 tetrahedral (A) and 32 octahedral (B) sites. Eight tetrahedral A-sites (8A) are occupied by half of the Fe^{3+} cations, whereas the rest of the Fe^{3+} and Ni^{2+} cations are distributed over the octahedral B-sites (16B) [16]. The cations distribution between A- and B-site is decided by the ionic radii, the nature of bonding and the synthesis technique. Thus, it is essential to develop an accurate technique for the preparation of ferrite nanomaterials with improved properties useful for varied devices fabrication.

Driven by this demand, we examined the influence of composition variation on the structures, morphology and magnetic properties of $Ni_{0.9}Cd_{0.1-x}Sr_xFe_2O_4$ (x = 0.00, 0.05 and 0.10) nanostructures synthesized via the simple auto-combustion method. As-prepared samples were thoroughly characterized at room temperature using diverse analytical tools. Results were analysed and discussed. Besides, a correlation between structural and magnetic properties was established.

* Corresponding author.
E-mail address: manojit.manojit.de1@gmail.com (M. De).

https://doi.org/10.1016/j.rinp.2019.102916
Received 24 June 2019; Received in revised form 26 December 2019; Accepted 26 December 2019
Available online 30 December 2019

Experimental procedures

Both pure as well as cadmium (Cd) and strontium (Sr) doped nickel (Ni) ferrite nanoparticles were prepared using auto-combustion method [17]. Highly pure (AR grade) stoichiometric amount of Ni, Cd, Sr and ferric nitrates was mixed in a beaker and heated for complete melting. Next, the citric acid at a molar ratio of 1:1 was added to this mixture before being heated to achieve absolute combustion. Burned agglomerated specimen was powdered using mortar pestle and then calcined at 800 ˚C for approximately 6 h. Afterward, the pellets form of the ferrite specimens were sintered at 850 ˚C for about 8 h.

X-ray diffraction (XRD) measurement (Rigaku SmartLab diffractometer) operated with Cu-K_α radiation of wavelength 1.54056 Å at scanning angle (2θ) in the range of 20˚ to 80˚ were performed to determine the structure and phases of synthesized nanoferrites. Besides, Rietveld analysis using PDXL software was carried out to refine the XRD data. Field-emission scanning electron microscope (FESEM, Carl Zeiss EVO 10, Japan) was used to image the surface morphology of nanoferrites. Energy dispersive X-ray (EDX, Oxford Instruments) measurement was conducted to detect the elemental composition of the studied samples. Raman spectra of the sintered samples in the wavenumber range of 130 to 800 cm^{-1} were recorded using STR-500 Micro-Raman spectrometer equipped with 532 nm diode laser source. Fourier transform infrared (FTIR) spectra were obtained (Shimadzu 8400S, Japan) using KBr as reference material. Magnetic properties of nanoferrites were measured by vibrating sample magnetometer (VSM, Model No. 4500EG, G Princeton Applied Research, USA) with a maximum magnetization field of 10 kOe. All the characterizations were carried out at room temperature.

Results and discussion

Phase, morphology, and structure of synthesized nano ferrites

Phase and structural analysis

Fig. 1 shows the XRD patterns of the as-synthesized specimens, which revealed a single phase with cubic structure. The lattice parameter (a) and the crystallite size (D) of all samples were evaluated (Table 1). Scherer's formula [18] was used to calculate the nanocrystallites size. With increasing substitution levels of Cd and Sr into the ferrite structures, the (3 1 1) XRD peak of all nanoferrites (except for $Ni_{0.9}Cd_{0.1}Fe_2O_4$) was shifted constantly towards higher angle accompanied by broadening. The observed broadening of the diffraction peak suggested the formation of tiny nanoparticles and related quantum size confinement. Furthermore, the lattice parameter of the prepared nickel ferrites was elongated linearly with the increase of Cd and Sr contents

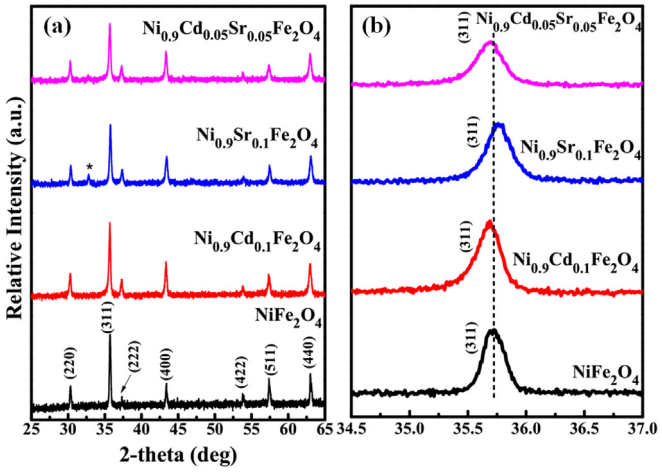

Fig. 1. XRD patterns of the synthesized samples [reproduced from Ref. [17]].

which was ascribed to the larger ionic radius of Cd compared to Sr. Besides, the sizes of nickel ferrite particles were shrunk and the lattice parameter was elongated with the increase in the substituent's contents (Table 1). The lattice parameters of the prepared ferrites were estimated using the expression [19]:

$$a = \frac{\lambda}{2}\frac{(h^2 + k^2 + l^2)}{Sin\theta} \quad (1)$$

where (hkl) signify the Miller indices, and θ denotes the diffraction angle corresponding to the (hkl) plane.

X-ray density (ρ_x) of the studied ferrites was calculated by Smith and Wijn formula [20]:

$$\rho_x = nM/Na^3 \quad (2)$$

where N is the Avogadro's number, n denotes the formula unit number present in the unit cell (n was equal to 8 for the proposed ferrites) and M represents the molecular weight of the specimens (Table 1).

The variation of L_A (the distance between magnetic ions so called the ion jump length in the tetrahedral A-site) and L_B (the distance between magnetic ions called the ion jump length in the octahedral B-site) was calculated using the relations [21]:

$$L_A = \frac{\sqrt{3}a}{4} \quad (3)$$

$$L_B = \frac{\sqrt{3}a}{2} \quad (4)$$

The calculated composition dependent values of L_A and L_B are enlisted in Table 1. The disclosed sensitivity of the ion jump lengths on the substituent Cd and Sr contents in the studied ferrites was attributed to the ionic radii mismatch assisted variation in the lattice constant [22].

The detailed phase analysis via PDXL Rietveld refinement program displayed that the proposed ferrite samples existed in a pure single phase (devoid of impurities). The observed value of R-factors and χ^2 that signified the goodness of the refinement (Fig. 2a–d) was obtained using:

$$R_p = \sum \frac{|y_{i(obs)} - y_{i(cal)}|}{\sum y_{i(obs)}} \quad (5)$$

$$R_{wp} = \sum \left| \frac{(y_{i(obs)} - y_{i(cal)})^2}{\sum y_{i(obs)}^2} \right|^{1/2} \quad (6)$$

$$\chi^2 = \sum \frac{(y_{i(obs)} - y_{i(cal)})^2}{n + p + c} \quad (7)$$

where, R_{wp} simply compare the calculated pattern to the data, n is the number of observations, p is the number of parameters and c is the number of constraints in the definition of goodness of fit. The quantitative analysis of the cubic phase was performed with split pseudo-Voigt function and the XRD pattern was fitted with whole powder pattern fitting (WPPF) program. Table 2 summarizes the calculated lattice parameters and refinement parameters of the studied samples. No other extra phases were detected in Reitveld analysis. There is no such structural phase change observed in introducing the foreign substituent atoms. The low values of χ^2 affirms the goodness of fitting.

It was acknowledged that when the A-site is substituted with different cations, the mismatch in the size can create non-uniform strain responsible for the unit cell deformation and hence the broadening in the XRD peak [23,24]. Williamson-Hall plots [25] were used to quantify such strain that could present in the specimen (Fig. 3). The strain (ε) was estimated from the slope of the straight line fit using the relation:

$$\beta Cos\theta = 4\varepsilon Sin\theta + \frac{k\lambda}{D} \quad (8)$$

where β is the full width at half maxima (FWHM) of the XRD peak positioned at θ, λ is the X-ray wavelength, D is nanocrystallite size and k

Table 1
Tables for various structural parameters calculated from XRD analysis.

Sample	a (Å)	ρ_x (g/cm^3)	V (Å^3)	D (nm)	L_A (Å)	L_B (Å)	ε (%)
$NiFe_2O_4$	8.329	5.3859	577.80	37	7.2131	5.8894	0.1730
$Ni_{0.9}Cd_{0.1}Fe_2O_4$	8.330	5.5104	578.01	36	7.2139	5.8901	0.2320
$Ni_{0.9}Sr_{0.1}Fe_2O_4$	8.489	5.1526	611.74	31	7.3516	6.0026	0.2074
$Ni_{0.9}Cd_{0.05}Sr_{0.05}Fe_2O_4$	8.342	5.4582	580.51	26	7.2243	5.8986	0.1692

is a constant called shape factor. The composition dependent alteration in the strain values of the prepared ferrites (Table 1) can be explained in terms of the valance state of the host material and the ionic radii of the substituted ions.

Morphology

Fig. 4(i) a–d shows the FESEM images of all the obtained nano-ferrites, which consisted of random distribution of agglomerated grains originated from the ignition of fuels during preparation. The grain size estimated from FESEM data was discerned to be larger than the one obtained from XRD analysis. This indicated that every grain was formed by the aggregation of several tiny ferrite nanocrystallites or nano-particles. It was asserted that the morphology of the microstructure is sensitive to the substituent contents. The elemental composition of the prepared ferrites was confirmed by EDX analysis. The EDX spectra displayed the homogeneous mixing of Ni, Cd, Sr, Fe and O atoms in the pure as well as doped nickel ferrites as shown in Fig. 4(ii) a–d. The measured composition was consistent with the calculated one.

Vibrational properties

Raman spectral analysis

Micro-Raman spectroscopy was used to characterize the phonon modes in the synthesized spinel ferrites [26]. Cubic spinel ferrites having the general formula of AB_2O_4 with $Fd\bar{3}m(O_h^7$ No. 227) group symmetry clearly disclosed five Raman active modes [27,28] assigned to A_{1g}, E_g and $3T_{2g}$ (Fig. 5). The notation A, E, and T signified the corresponding one, two and three-dimensional representations of phonon modes, and g designated the center of inversion symmetry [29]. The A_{1g} mode was allocated to the symmetric stretching of oxygen atoms in the tetrahedral sites along Fe–O (and Ni–O) bonds termed as tetrahedral breathing mode (TBM). Furthermore, E_g mode was assigned to the symmetric bending of oxygen with regard to the metal ion and $T_{2g}(3)$ mode was approved to the asymmetric bending of oxygen bond. The $T_{2g}(2)$ mode was allotted to the asymmetric stretching of Fe (Ni) and O. Meanwhile, the $T_{2g}(2)$ and $T_{2g}(3)$ modes were endorsed to the vibrations associated with the octahedral group. The mode $T_{2g}(1)$ was allocated to the translational movement of the tetrahedron (metal ion at the tetrahedral site plus oxygen atoms). Moreover, the displacement of metal atoms in modes A_{1g}, E_g and $T_{2g}(3)$ was insignificant. In ferrites, the vibration modes that appear beyond 600 cm^{-1} are generally allocated to the motion of the oxygen atoms in the tetrahedral AO_4 group and those occur lower than 600 cm^{-1} are assigned to the motion of the oxygen atoms in the octahedral BO_6 group [30].

In this present study, the Cd and Sr substituted $NiFe_2O_4$ compounds having an inverse or partially inverse spinel structures displayed some extra Raman modes (Table 3). The emergence of such extra vibrational modes as spectral peaks was assigned to the existence of non-equivalent

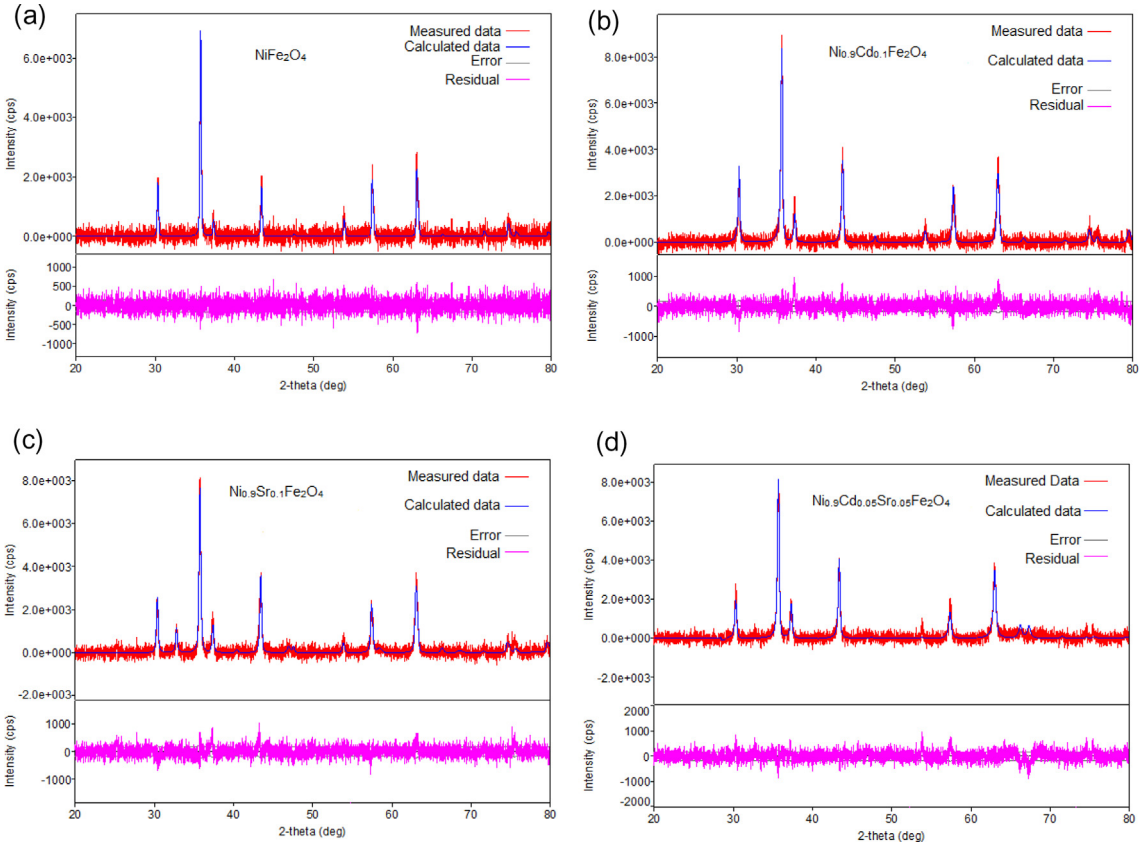

Fig. 2. Rietveld analysis of (a) $NiFe_2O_4$, (b) $Ni_{0.9}Cd_{0.1}Fe_2O_4$, (c) $Ni_{0.9}Sr_{0.1}Fe_2O_4$ and (d) $Ni_{0.9}Cd_{0.05}Sr_{0.05}Fe_2O_4$.

Table 2
Structural parameters for pure and doped nickel ferrites obtained via Rietveld refinement procedure.

Sample	Space Group	Lattice Parameter (Å)	Refinement Parameters				ICDD Card Number
			R_{wp}	R_p	S	χ^2	
$NiFe_2O_4$	Fd-3m	8.350(3)	6.3	5.03	1.0304	1.0618	01-078-3741
$Ni_{0.9}Cd_{0.1}Fe_2O_4$	Fd-3m	8.350(1)	4.35	3.45	1.0944	1.1977	01-005-8429
$Ni_{0.9}Sr_{0.1}Fe_2O_4$	Fd-3m	8.326(2)	5.21	3.73	1.3355	1.7834	01-014-8286
$Ni_{0.9}Cd_{0.05}Sr_{0.05}Fe_2O_4$	Fd-3m	8.325(7)	5.31	3.5	1.3811	1.9073	01-054-0964

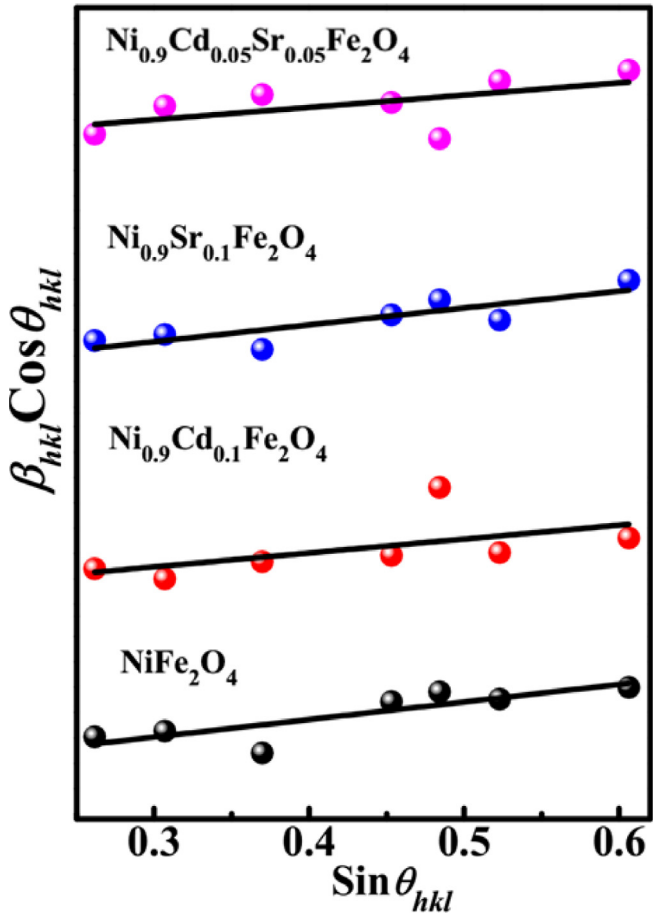

Fig. 3. Williamson-Hall plots for all studied nanoferrite compositions.

atoms at the octahedral B-sites which were occupied by either Fe or Ni ions or by the substituted Cd or Sr ions in the modified $NiFe_2O_4$ nanostructures [31]. The mismatch in the ionic radii of Ni, Fe and substituent ions produced a wide variation in the bond lengths formed between Fe/Ni/substituent atoms and oxygen. This broad distribution in the bond lengths could result in extra Raman peaks, wherein these peaks were assigned to the unit cell with Ni ions occupancy at the octahedral site and the other was approved to the unit cell with Ni ions occupation both at the octahedral and tetrahedral sites. It was affirmed that the occurrence of such doublet-like peaks in the Raman spectra towards the lower wavenumber region could be due to the existence of a mixed spinel phase in the ferrite nanostructures [32].

FTIR spectra

Fig. 6 depicts the FTIR spectra of all ferrite samples recorded in the wavenumber range of 450–3700 cm^{-1}. The IR spectra provided useful information related to the substituent atoms assisted deformation in the spinel structure, bonding vibrations (vibrational modes), end of chemical reaction, ionic positions in the ferrite nano-crystal, and distribution of cations in the ferrite unit cell [33]. Generally, normal and inverse cubic spinel phase of ferrites reveal four significant absorption bands and two fundamental bands (υ_1 andυ_2). In the present case, the observed two prominent absorption bands at 600 cm^{-1} (υ_1) and 400 cm^{-1} (υ_2) were allocated respectively to the intrinsic stretching vibrations of the tetrahedral and octahedral sites which confirmed the existence of the cubic spinel phase in the studied nanoferrites [34].

It is known that the octahedral sites in pure nickel nanoferrites ($NiFe_2O_4$) are occupied by Ni ions, whereas in doped nickel nanoferrites ($Ni_{0.9}Cd_{0.1}Fe_2O_4$ and $Ni_{0.9}Sr_{0.1}Fe_2O_4$) such sites are occupied by Ni^{2+} and Cd^{2+}as well as Ni^{2+} and Sr^{2+}. Conversely, in $Ni_{0.9}Cd_{0.05}Sr_{0.05}Fe_2O_4$ the octahedral sites are occupied by Ni, Cd and Sr ions, while both the tetrahedral and the octahedral sites are partially occupied by Fe ions [35]. Thus, the bands appeared at lower wave numbers (435, 439, 438, and 439 cm^{-1}) were due to the octahedral group complexes while those occurred at higher wavenumbers (601, 613, 599 and 600 cm^{-1}) were due to the tetrahedral group complexes (Table 4) [36]. Meanwhile, the values of υ_1 and $\upsilon_2$were shifted towards higher wavenumber with the increase in the substituent contents [37]. The variations in the absorption peak positions and intensities were decided by the metal cations mass and the bond strength between the metal cations and the oxygen atoms [38]. Usually, for solid materials the IR absorption bands in the wavenumber range of 100–1000 cm^{-1} are allocated to ionic vibrations in the crystalline lattice sites. Herein, the observed absorption band at 3388 cm^{-1} was aroused from the O–H stretching vibrational modes associated to the water molecule and the band around 2930 cm^{-1} was due to the O–H group in the citric acid. Additionally, the band at 1450 cm^{-1} was approved to the asymmetric stretching vibrations of NO_3 and the one around 1647 cm^{-1} was allotted to the vibration of carbo-oxalate anions [39]. The appearance of a band at 2352 cm^{-1} was due to the stretching vibration of the hydroxyl group present in the nanoferrites.

The force constant was found to enhance with the increase of doping contents in the nanoferrites (Table 4), indicating the inter-ionic bond strengthening. The value of force constant for the tetrahedral site of $Ni_{0.9}Cd_{0.1}Fe_2O_4$ was maximum due to its higher atomic weight. The disparities in the distances between Fe^{3+} and O^{2-} ions involving the octahedral and tetrahedral complexes of $Ni_{0.9}Cd_{0.1}Fe_2O_4$ caused appreciable variation in the FTIR absorption bands position. The force constant of the octahedral (k_O) and tetrahedral site (k_t) was calculated using the relations [40]:

$$k_t = 4\pi^2 C^2 M_t \nu_t^2 \quad (9)$$

$$k_O = 4\pi^2 C^2 M_O \nu_O^2 \quad (10)$$

where υ_t and υ_o denotes the frequency of vibrational bands originate from the tetrahedral and octahedral sites, M_O and M_t represent the corresponding molecular weights [41,42] and C is the speed of light in vacuum.

Magnetic properties

Fig. 7 displays the magnetic response of all the studied nanoferrites. The magnetic measured properties of the synthesized ferrites such as

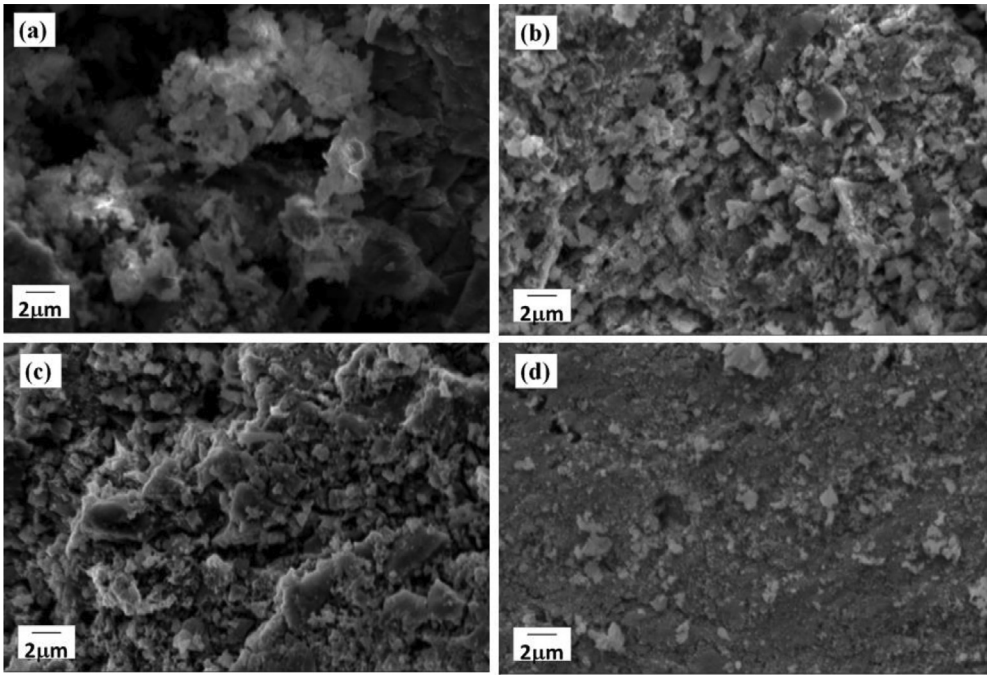

Fig. 4. (i) FESEM images of the prepared samples revealing porous and non-uniform granular morphology of (a) $NiFe_2O_4$, (b) $Ni_{0.9}Cd_{0.1}Fe_2O_4$, (c) $Ni_{0.9}Sr_{0.1}Fe_2O_4$ and (d) $Ni_{0.9}Cd_{0.05}Sr_{0.05}Fe_2O_4$. (ii) The EDX spectra of (a) $NiFe_2O_4$,(b) $Ni_{0.9}Cd_{0.1}Fe_2O_4$, (c) $Ni_{0.9}Sr_{0.1}Fe_2O_4$ and (d) $Ni_{0.9}Cd_{0.05}Sr_{0.05}Fe_2O_4$.

saturation magnetization (M_s), remanent magnetization (M_r), coercive field (H_c), squareness ratio (M_r/M_s), and the magnetic moment (η_t^B) are summarized in Table 5. The values of M_s for Cd^{2+}, Sr^{2+}, and Cd^{2+}-Sr^{2+} substituted $NiFe_2O_4$ was increased from 18.34 emu/g to 34.79 emu/g. Following Yafet-Kittel [43,44], the magnetic behavior disclosed by the studied ferrites was interpreted via two sub-lattice collinear model [45,46] and three sub-lattice non-collinear models. For spinel ferrite structure, the two sub-lattice model deals with three kinds of super-exchange interactions such as A-A, B-B, and A-B, where the strength of A-B exchange interaction is higher than A-A and B-B [47]. The observed large value of net magnetic moment $\eta_t^B = M_B - M_A$ in the studied composition clearly indicated the occurrence of the higher value of M_s. The experimental value of the magnetic moment per formula unit was calculated in terms of the molecular weight (M_W) of the synthesized ferrite nanoparticles via the expression [48]:

$$\eta_B^e = \frac{M_W M_S}{5585} \tag{11}$$

According to two sub-lattice model, the octahedral (B) sites are occupied by eight divalent metal ions (Me^{2+}), whereas other sixteen Fe^{3+} ions are equally distributed among A and B-site with a cation distribution given by $[Fe^{3+}]_A[Me^{2+}Fe^{3+}]_BO_4$. In the proposed spinel

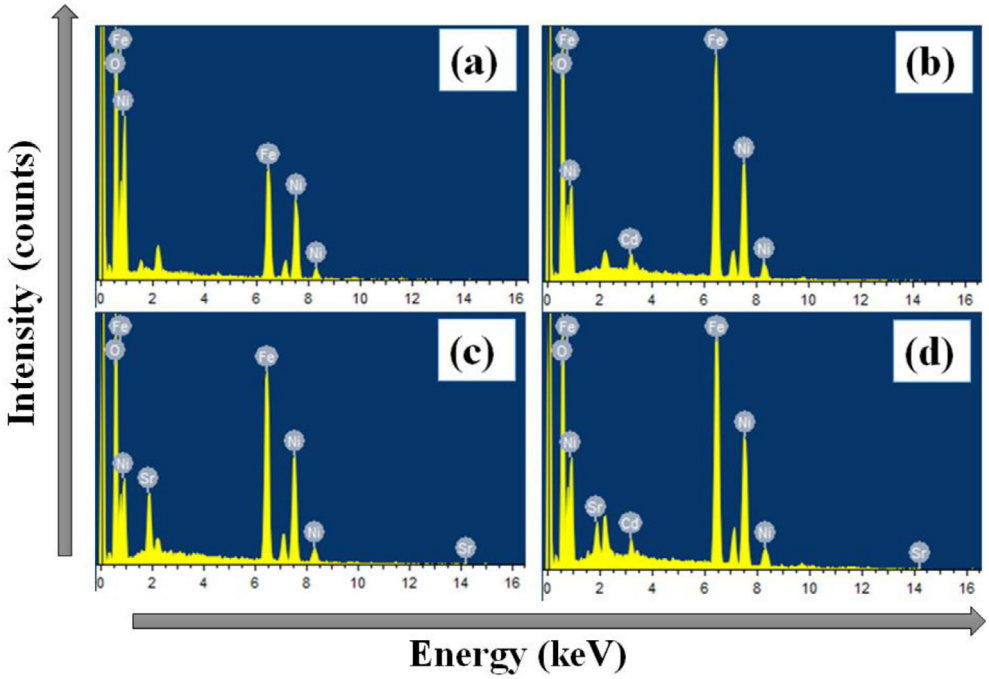

Fig. 4. (*continued*)

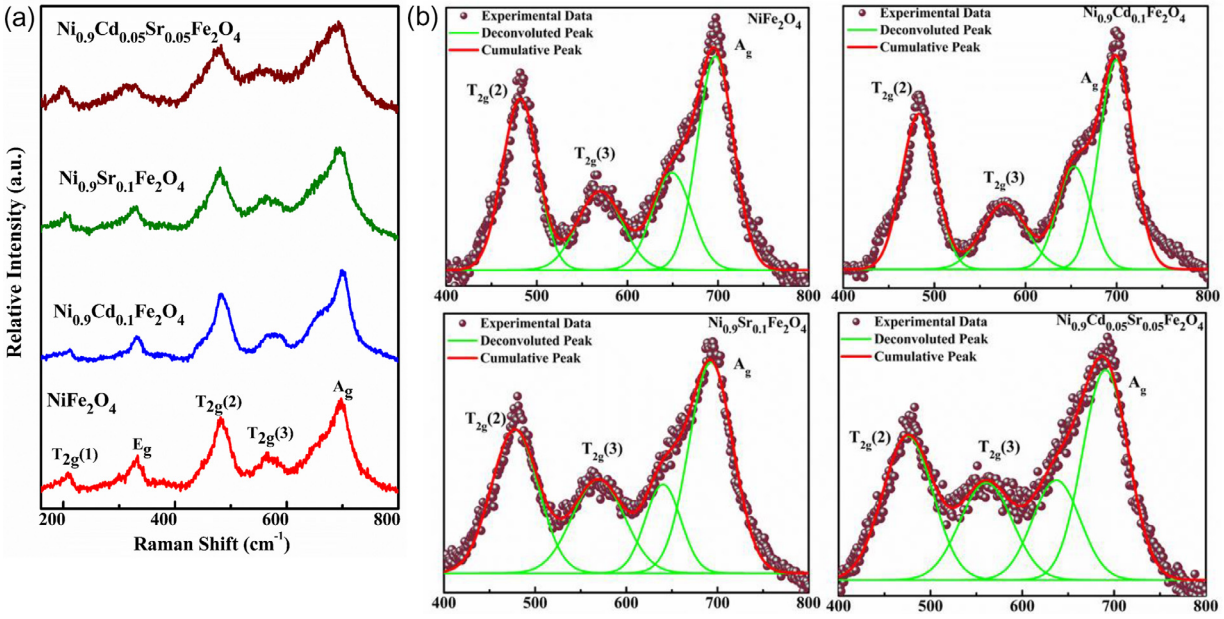

Fig. 5. (a) Raman spectra of all samples and (b) the corresponding deconvoluted Raman modes in the range of 400–800 cm^{-1} [reproduced from Ref. [17]].

Table 3
All the studied samples and the corresponding Raman vibrational modes.

Sample	$T_{2g}(1)$	E_g	$T_{2g}(2)$	$T_{2g}(3)$	A_g
$NiFe_2O_4$	210	331	481	566	696
$Ni_{0.9}Cd_{0.1}Fe_2O_4$	212	331	482	574	700
$Ni_{0.9}Sr_{0.1}Fe_2O_4$	202	329	480	564	694
$Ni_{0.9}Cd_{0.05}Sr_{0.05}Fe_2O_4$	196	312	479	551	692

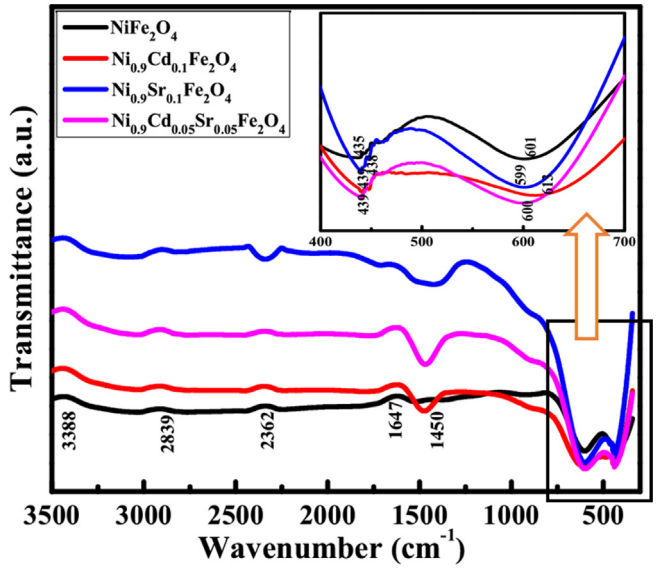

Fig. 6. FTIR spectra of all the proposed nanoferrites. Inset shows the main two peaks for octahedral and tetrahedral sites of ferrites.

Table 4
Absorption band and force constant for all studies samples.

Composition	υ_1 (cm^{-1})	υ_2 (cm^{-1})	k_t (10^2 N/m)	k_O (10^2 N/m)
$NiFe_2O_4$	601	435	2.64	1.39
$Ni_{0.9}Cd_{0.1}Fe_2O_4$	613	439	2.75	0.95
$Ni_{0.9}Sr_{0.1}Fe_2O_4$	599	438	2.63	0.94
$Ni_{0.9}Cd_{0.05}Sr_{0.05}Fe_2O_4$	600	439	2.63	1.06

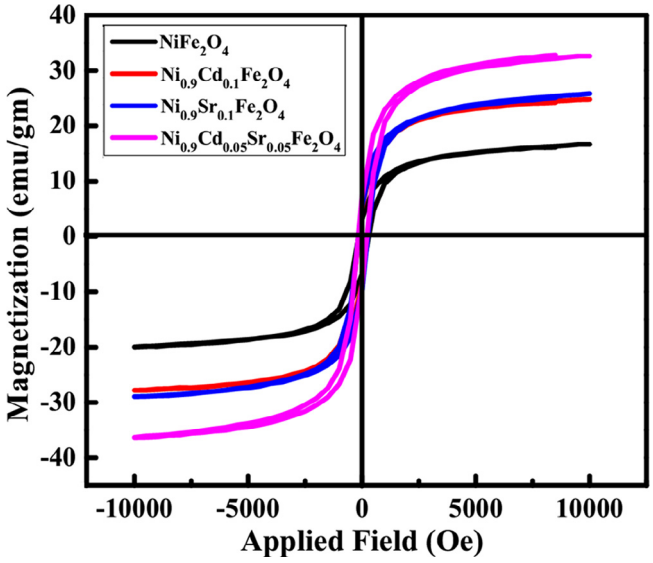

Fig. 7. Room temperature magnetic hysteresis loops of pure $NiFe_2O_4$ and substituted nickel ferrites.

ferrite nanostructure ($NiFe_2O_4$), the possible cations distribution could be $[Fe^{3+}_{1.0}]_A[Ni^{2+}_{1.0}\ Fe^{3+}_{1.0}]_B\ O_4{}^{2-}$. The substituted Cd^{2+} (with zero magnetic moments) and Sr^{2+} ions in the lattice showed a strong preference to occupy A-site and thereby the cation distribution in the three compositions was configured as [49]:

$$Ni_{0.9}Cd_{0.1}Fe_2O_4 \rightarrow (Cd^{2+}_{0.1}Fe^{3+}_{0.9})_A[Ni^{2+}_{0.9}Fe^{3+}_{1.1}]_BO_4^{2-}$$

$$Ni_{0.9}Sr_{0.1}Fe_2O_4 \rightarrow (Sr^{2+}_{0.1}Fe^{3+}_{0.9})_A[Ni^{2+}_{0.9}Fe^{3+}_{1.1}]_BO_4^{2-}$$

$$Ni_{0.9}Cd_{0.05}Sr_{0.05}Fe_2O_4 \rightarrow (Cd^{2+}_{0.05}Sr^{2+}_{0.05}Fe^{3+}_{0.9})_A[Ni^{2+}_{0.9}Fe^{3+}_{1.1}]_BO_4^{2-}$$

Fundamentally, the replacement of any dopant ions in the $NiFe_2O_4$ lattice could significantly influence the magnetization. The mechanism of the alteration of magnetization due to the occupation of substituent ions was understood as follows: the Fe^{3+} ions with stronger magnetic moment (5 μ_B) were replaced by Cd^{2+} ions and Sr^{2+} (both with the weaker magnetic moment of 0 μ_B), thereby the magnetic moment of A-site was reduced and that of B-site was enhanced. Furthermore, the

Table 5
Table for various room temperature magnetic parameters.

Sample	M_s (emu/g)	M_r (emu/g)	H_c (G)	$\frac{M_r}{M_s}$	η_B^{obs}	α_{YK}	K (erg/Oe)	μ_i
$NiFe_2O_4$	18.342	5.0198	218.59	0.2736	0.0420	0	4176.43	2.9812
$Ni_{0.9}Cd_{0.1}Fe_2O_4$	26.303	6.9030	183.50	0.2624	0.0429	34.32	5027.70	4.9538
$Ni_{0.9}Sr_{0.1}Fe_2O_4$	27.389	7.6299	203.03	0.2785	0.0424	34.33	5792.48	4.0146
$Ni_{0.9}Cd_{0.05}Sr_{0.05}Fe_2O_4$	34.794	7.9673	188.87	0.2289	0.0427	24.11	6845.35	4.5981

observed enhancement in the saturation magnetization (M_s) was interpreted in terms of the increased super-exchange interaction within the inter-sub-lattice (A-B), which was consistent with the collinear two sub-lattice model.

The Bohr magneton (μ_B), constant for the magneto-crystalline anisotropy (K) and the initial permeability (μ_i) was calculated using the relations [50]:

$$K = \frac{H_c \times M_s}{0.96} \tag{12}$$

$$\mu_B = \frac{M \times M_s}{5585} \tag{13}$$

$$\mu_i = \frac{M_s^2 \times D}{K} \tag{14}$$

where the symbols have their usual meaning.

The estimated value of M_s and μ_B exhibited an increasing trend which was ascribed to the existence of strong exchange interactions among the ions that occupied the tetrahedral and the octahedral sites. The shortening in the lattice parameter also confirmed the emergence of strong ionic interactions among various lattice sites. Perusal of Table 5 enlists the composition dependent alterations in the values of K and μ_B together with other magnetic parameters. Fluctuations in grain size may also have impact on magnetization due to domain wall movement under the action of magnetic field. The overall value of magnetization obtained is a result of the contributions of all the factors depending upon ferrite composition. Pure nickel ferrite ($NiFe_2O_4$) disclosed the lowest value of initial permeability and Cd/Sr substituted one showed the highest value.

Conclusions

Tailoring the room temperature structural, morphological, vibrational and magnetic properties of pure as well as Cd and Sr ions substituted nickel nanoferrites were assessed in this communication. The X-Ray diffraction pattern of $Ni_{0.9}Cd_{0.1-x}Sr_xFe_2O_4$ (x = 0.00, 0.05 and 0.10) ferrites synthesized by self-ignited auto-combustion method gives a clear indication of formation of cubic spinel phase with Scherrer's grain diameter ranging from 26 to 37 nm. Rietveld analysis revealed the formation of the single spinel ferrite phase without having any residual phase formation and structural transition. The lattice parameter of the studied nanoferrites were ranged from 8.32 Å to 8.48 Å. Overall, the properties of the proposed nanoferrites were found to be sensitive to the ionic radii of substituent ions. The porous morphology of nanoferrites which is manifested by FESEM study, is beneficial for gas sensing applications. EDX spectra detected the appropriate stoichiometric elemental compositions. Raman spectra of the obtained spinel ferrites disclosed five typical phonon modes (A_{1g} + E_g + $3T_{2g}$) which are signature of spinel structure. Both FTIR band positions and intensities related to tetrahedral and octahedral sites were sensitive to the substitution contents. The magnetic properties of the studied nanoferrites were enhanced due to the incorporation of substituent ions in the A-site of the spinel lattice, exhibiting a maximum for $Ni_{0.9}Sr_{0.05}Cd_{0.05}Fe_2O_4$ composition. The value of the coercive field was reduced with the increase of doping levels.

Authors' contribution

RT has prepared the samples. The experiment related to XRD, FE-SEM, EDX, Raman, FTIR and magnetic measurement were accomplished by RT and MD. The data analysis and manuscript written carried out by both RT and MD. The whole work was supervised by HST and SKG.

Declaration of Competing Interest

The authors declare that they have no known competing financial interests or personal relationships that could have appeared to influence the work reported in this paper.

Acknowledgments

Authors are thankful to the Department of Pure and Applied Physics, Guru Ghasidas Vishwavidyalaya for facilities. Financial assistance from the University Grant Commission (UGC, India) through MRP grant (F. No. 41-954/2012(SR)) and GUP/RU/UTM Vot. 18H68 and KPT/FRGS 5F050 are greatly appreciated. RT and MD are indebted to UGC for providing Ph.D. research fellowship.

Appendix A. Supplementary data

Supplementary data to this article can be found online at https://doi.org/10.1016/j.rinp.2019.102916.

References

[1] Zhou KB, Wang X, Sun XM, Peng Q, Li YD. Enhanced catalytic activity of ceria nanorods from well-defined reactive crystal planes. J Catal 2005;229:206–21.
[2] Singhal S, Chandra K. Cation distribution and magnetic properties in chromium substituted nickel ferrites prepared using aerosol route. J Solid State Chem 2007;180:296–300.
[3] Ebrahimi SAS, Azadmanjiri J. Evaluation of $NiFe_2O_4$ ferrite nano-crystalline powder synthesized by a sol-gel auto-combustion method. J Non-Cryst Solids 2007;353:802–4.
[4] Kumar KV, Paramesh D, Reddy PV. Effect of aluminum doping on structural and magnetic properties of Ni-Zn ferrite nanoparticles. World J Nano Eng 2015;5:68–77.
[5] Gul IH, Pervaiz E. Comparative study of $NiFe_{2-x}Al_xO_4$ ferrite nanoparticles synthesized by chemical co-precipitation and sol–gel combustion techniques. Mater Res Bull 2012;47:1353–61.
[6] Anwar MS, Ahmed Faheem, Koo Bon Heun. Enhanced relative cooling power of $Ni_{1-x}Zn_xFe_2O_4$ ($0.0 \le x \le 0.7$) ferrites. Acta Mater 2014;71:100–7.
[7] Domenichini B, Caillot T. Sintering of Fe_2NiO_4 with an internal binder: a way to obtain a very dense material. Acta Mater 2003;51:4815–21.
[8] Balaji M, Jeyaram RA, Chandrasekaran S, Maheswari LB. Effect of Mn^{2+} substitution on the structural, morphological and magnetic properties of copper ferrite nanoparticles. Mater Techno 2017;32(6):378–84.
[9] Caizer C, Popovici M, Savii C. Spherical $(Zn_8Ni_{1-8}Fe_2O_4)_\gamma$ nanoparticles in an amorphous $(SiO_2)_{1-\gamma}$matrix, prepared with the sol-gel method. Acta Mater 2003;51:3607–16.
[10] Chen DH, He XR. Synthesis of nickel ferrite nanoparticles by a sol-gel method. Mater Res Bull 2001;36:1369–77.
[11] Stoia M, Barvinschi P, Tudoran LB, Barbu M, Stefanescu M. Synthesis of nanocrystalline nickel ferrite by thermal decomposition of organic precursors. J Therm Anal Calorim 2012;108:1033–9.
[12] Naseri MG, Saion EB, Ahangar AH, Hashim M, Shaari AH. Simple preparation and characterization of nickel ferrite nanocrystals by a thermal treatment method. Powder Technol 2011;212:80–8.
[13] Joshi S, Kumar M, Chhoker S, Srivastava G, Jewariya M, Singh VN. Structural, magnetic, dielectric and optical properties of nickel ferrite nanoparticles synthesized by co-precipitation method. J Mole Struct 2014;1076:55–62.

[14] Bućko MM, Haberko K. Hydrothermal synthesis of nickel ferrite powders, their properties and sintering. J European Ceram Soc 2007;27:723–7.
[15] Zhang Z, Yao G, Zhang X, Lin H. Synthesis and characterization of nickel ferrite nanoparticles via planetary ball milling assisted solid-state reaction. Ceram Int 2015;41(3):4523–30.
[16] Li F, Liu J, Evans DG, Duan X. Stoichiometric synthesis of pure MFe2O4 (M = Mg Co, and Ni) spinal ferrites from tailored layered double hydroxide (hydrotalcite-like) precursors. Chem Mater 2004;16:1597–602.
[17] De M, Rout A, Tewari HS. Synthesis and structural characterization of A-site doped NiFe2O4. AIP Conference Proceedings 2017;1837040042.
[18] Scherrer P. Determination of the internal structure and size of colloid particles by X-rays. Colloid Chemistry A textbook. Chemical technology in individual re-presentations. Berlin, Heidelberg: Springer; 1912. p. 387–409.
[19] Cullity BD. Elements of X-ray Diffraction. Philippines: Addison-Wesley Publishing Company, Inc.; 1978. p. 284.
[20] Smit J, Wijn HPJ. Ferrites. New York: John Wiley; 1959.
[21] Gabal MA, Angari YMA. Effect of chromium ion substitution on the electromagnetic properties of nickel ferrite. Mater Chem Phys 2009;118:153–60.
[22] Anupama MK, Rudraswamy B, Dhananjaya N. Investigation on impedance response and dielectric relaxation of Ni-Zn ferrites prepared by self-combustion technique. J Alloys Compd 2017;706:554–61.
[23] Lennox RC, Price MC, Jamieson W, Jura M, Aladine AD, Murray CA, et al. Strain-driven structural phase transformations in dysprosium doped $BiFeO_3$ ceramics. J Mater Chem C 2014;2:3345–60.
[24] De M, Patel SP, Tewari HS. Strain-induced structural phase transition in $NaNbO_3$ doped $BiFeO_3$. J Mater Sci: Mater Electron 2017;28:6928–35.
[25] Williamson GK, Hall WH. X-ray line broadening from filed aluminum and Wolfram. Acta Metall 1953;22–31.
[26] Das RS, Agrawal YK. Raman spectroscopy: recent advancements, techniques, and applications. Vib Spectrosc 2011;57:163–76.
[27] Hosterman BD. Raman Spectroscopic Study of Solid Solution, Spinel Oxides August PhD. thesis Las Vegas: University of Nevada; 2011.
[28] Pradhan DK, Mishra P, Puli VS, Satyaprakash Sahoo, Pradhan DK, Katiyar RS. Synthesis and structural characterization of A-site doped $NiFe_2O_4$. J Appl Phys 2014;115:243904.
[29] Prince E. Mathematical technique in crystallography and material science. New York, Heidelberg, Berlin: Springer Verlag; 1982.
[30] Ahlawat A, Sathe VG. Raman study of $NiFe_2O_4$ nanoparticles, bulk and films: effect of laser power. J Raman Spectroscopy 2011;42:1087–94.
[31] Wang Z, Lazor P, Saxena SK, St H, O'Neill C. High-pressure Raman spectroscopy of ferrite $MgFe_2O_4$. Mater Res Bull 2002;37:1589–602.
[32] Phong PT, Nam PH, Phuc NX, Huy BT, Lu LT, Manh DH. In-Ja LeeEffect of Zinc concentration on the structural, optical and magnetic properties of mixed Co-Zn ferrites nanoparticles synthesized by low temperature Hydrothermal method. Metall Mater Trans A 2019;50A:1571–81.
[33] Zhou ZH, Xue JM, Wang J. $NiFe_2O_4$ nanoparticles formed in situ in a silica matrix by mechanical activation. J Appl Phys 2002;91:6015–20.
[34] Jacob BP. On the structural, magnetic, electric properties of dysprosium doped Cu-Zn mixed ferrite nanoparticles. J Alloys Compd 2013;578:314–9.
[35] Lodhi YM. New $Mg_{0.5}Co_xZn_{0.5-x}Fe_2O_4$ nano-ferrites: a structural elucidation and electromagnetic behavior evaluation. Curr Appl Phys 2014;14(5):716–20.
[36] Malik H. Influence of cobalt substitution on the magnetic properties of zinc nano-crystals synthesized via micro-emulsion route. Ceram Int 2014;40(7):9439–44.
[37] Hashim M. Synthesis and characterizations of Ni^{2+} substituted cobalt ferrite na-noparticles. Mater Chem Phys 2014;139:364–74.
[38] Mohit K, Gupta VR, Gupta N, Rout KS. Structural and microwave characterization of $Ni_{0.2}Co_xZn_{0.8-x}Fe_2O_4$ for antenna applications. Cream Int 2014;40(1):1575–86.
[39] Nisari MA, Davar F, Mahmoudi T. A simple route to synthesize nanocrystalline nickel ferrite ($NiFe_2O_4$) in the presence octanoic acid as a surfactant. Polyhydron 2009;28(8):1455–8.
[40] De M, Mukherjee A, Tewari HS. Characterization of cadmium substituted nickel ferrites prepared using the auto-combustion technique. Process Appl Ceram 2015;9(4):193–7.
[41] Ditta A, Khan MA, Junaid M, ArifKhalil RM, Warsi MF. Structural magnetic and spectral properties of Gd and Dy co-doped dielectrically modified Co-Ni ($Ni_{0.4}Co_{0.6}Fe_2O_4$) ferrites. Physica B 2017;507:7493–7.
[42] Neel L, C. R. Acad. Sci. Paris 230; 1950. p. 375.
[43] Ponpandian N, Narayanasamy A, Chinnasamy CN, Sivakumar N, Greneche JM, Chattopadhyay K, et al. Néel temperature enhancement in nanostructured nickel zinc ferrite. Appl Phys Lett 2005;86:192510.
[44] Yafet Y, Kittel C. Anti-ferromagnetic arrangements in ferrites. Phys Rev 1952;87:290.
[45] Raju K, Venkataiah J, Yoon DH. Effect of Zn substitution on the structural and magnetic properties of Ni-Co ferrites. Ceram Int 2014;40:9337.
[46] Jadhav J, Biswas S, Yadav AK, Jha SN. Structural and magnetic properties of nano-crystalline Ni-Zn ferrites: in the context of cationic distribution. J Alloy Compd 2017;696:28–41.
[47] Jiangtao Wu, Liao Zuzhen, Sun Ting, Lun-Wei Su, Bi Jian, Fan Guangyin, et al. Tunable magnetic pole inversion in multiferroic $BiFeO_3$–$DyFeO_3$ solid solution. J Mater Chem C 2017;5:4063–7.
[48] Krishna KR, Kumar KV, Gupta CR, Ravinder D. Magnetic properties of Ni-Zn ferrites by citrate gel method. Adv Mater Phys Chem 2012;2:149–54.
[49] Yuan Qiao, Pan Linlin, Liu Run, Wang Jingming, Liao Zuzhen, Qin Lili, et al. Cation distribution and magnetism in quenched ZnFe2O4. J Electron Mater 2018;47(7):3608.
[50] Bahiraei H, Shoushtari MZ, Gheisari K, Ong CK. The effect of sintering temperature on the electromagnetic properties of nano-crystalline Mg Cu Zn ferrite prepared by sol-gel auto combustion method. Mater Lett 2014;122:129–32.